THE ASTROPHYSICAL JOURNAL, 362:624–633, 1990 October 20

OBSERVATIONS AND SHOCK MODELS OF THE JET AND HERBIG-HARO OBJECTS HH 46/47

PATRICK HARTIGAN[1] AND JOHN RAYMOND[1]
Harvard-Smithsonian Center for Astrophysics

AND

JOHN MEABURN
Department of Astronomy, University, of Manchester
Received 1990 February 2; accepted 1990 April 19

ABSTRACT

We present new monochromatic images, long-slit echelle spectra, and theoretical position-velocity diagrams of the Herbig-Haro objects HH 46 and HH 47. The outer bow shock HH 47D extends almost all the way back to the infrared source driving the outflow in a narrow-band [O II] image of the region, but is not easily visible in Hα and [S II]. We confirm the discovery of a counterjet in [S II] reported by Reipurth. Long-slit spectra of HH 47D show a "hook" shape in position-velocity space which can be understood in terms of a spatially resolved bow shock moving at an angle roughly 45° to the line of sight. The object HH 47A at the end of the jet also appears to be a bow shock rather than a Mach disk as has been suggested previously. The presence of *two* bow shocks within a single outflow is not predicted from a simple continuous jet model, but can be understood if the outflow is episodic or if both a disk wind and a stellar wind are present in the system.

Subject headings: nebulae: internal motions — shock waves — stars: pre–main-sequence

I. INTRODUCTION

Supersonic flows from young stars have been the focus of much observational and theoretical work in the last decade. Deep CCD images of star formation regions (e.g., Mundt, Brugel, and Bührke 1987) have shown that many young stellar objects (YSOs) eject highly collimated outflows that become visible as jets and Herbig-Haro objects when radiative shocks are present. Theoretical simulations of jets indicate that a variety of radiative shocks can occur both along the jet and in the area of the "working surface" where the jet material collides with the ambient medium (Norman, Smarr, and Winkler 1985; Lind *et al.* 1989). The two strongest shocks in a jet are typically the outer bow shock, which compresses and heats the ambient medium, and a Mach disk or annular shock that decelerates the outflowing jet.

HH objects and stellar jets are often several arcseconds in size, making it possible to obtain spatially resolved velocity profiles of the emitting gas. Such observations provide a *quantitative* test for any shock model of stellar jets and Herbig-Haro objects. A simple bow shock model has proved effective in explaining the spatial and velocity structure of several HH objects (Raga and Böhm 1986; Hartigan, Raymond, and Hartmann 1987, hereafter HRH). If the flow is more or less continuous, then there should be a Mach disk where the jet collides with the ambient medium, and both the Mach disk and the bow shock should be visible for typical stellar jet parameters (Hartigan 1989). Episodic jets (essentially "bullets"; Norman and Silk 1979) may not have Mach disk emission, but they should exhibit multiple bow shocks as later ejections plow into the wakes of the earlier ones.

It is important to establish whether observations of jets demonstrate unambiguous evidence for episodic flows. Bipolar outflows from YSOs contain large amounts of energy and momentum (Lada 1985) and are difficult to explain in terms of a simple stellar wind. Some theoretical models have attempted to use a magnetic accretion disk to drive YSO flows (Pudritz and Norman 1983; Königl 1989). If accretion and outflow are related, as some studies indicate (e.g., Cabrit *et al.* 1990), then episodic outflow indicates nonsteady disk accretion and may be related to eruptive FU Orionis outbursts (Kenyon and Hartmann 1988). Reipurth (1989*a*) has suggested that multiple ejections occur in the HH 111 flow, and Reipurth (1989*b*) employs a similar explanation for his spectrum of HH 47.

HH 46 and HH 47 are particularly well suited for intensive study, since these objects outline a flow from a single, isolated globule and can be observed without the confusion of overlapping outflows. A bright infrared source at the center of the globule ($L_* \sim 15\ L_\odot$; Emerson *et al.* 1990; Sahu, Sahu, and Pottasch 1989; Graham and Heyer 1989) excites a reflection nebula and drives a highly collimated jet into the surrounding medium (Graham and Elias 1983; Dopita, Binette, and Schwartz 1982). The jet and HH objects extend over several arcminutes in the sky, making spatially resolved observations of the emission lines fairly straightforward.

In this paper we present new CCD images and high-resolution line profiles of the HH 46/47 system. We determine the location, velocity, and orientation of the principal shocks in the system by comparing the observed and theoretical position-velocity diagrams for spatially resolved radiative bow shocks. The models and observations presented below provide quantitative evidence for *two* bow shocks in the HH 47 flow, consistent with a multiple ejection scenario or a disk wind model, but in disagreement with a continuous jet model.

II. OBSERVATIONS

The images in this paper were obtained 1989 April 25 and 26 with the TI2 CCD at the prime focus of the 4 m telescope atop

[1] Visiting Astronomer, Cerro Tololo Inter-American Observatory, operated by the National Optical Astronomy Observatory under contract to the National Science Foundation.

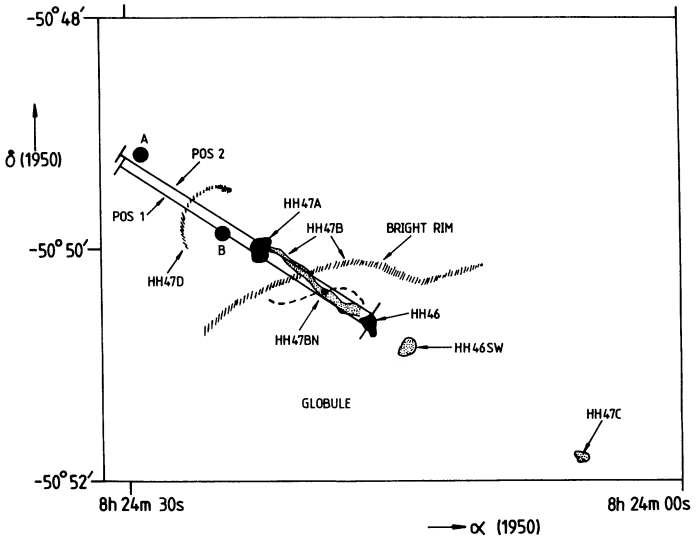

FIG. 2.—Identification sketch of the HH 46/47 region, showing the principal HH objects in the area and the positions of the slit used for the spectroscopic observations (see also Fig. 1). The secondary jet (*dashed line*) suggested by Glencross *et al.* (1989) is likely to be a continuation of the reflection nebula surrounding the infrared source.

Cerro Tololo. The plate scale was 0.″6 per pixel, providing a field of view of 4.′0 × 4.′0 for a single frame. Several frames co-added together make up the final images displayed in Figure 1 (Plate 29). The object identifications in Figure 2 follow those published by Scarrott and Warren-Smith (1988). The center wavelengths and bandpasses for the [O II], Hα, and [S II] filters were 3727 Å (21 Å), 6563 Å (17 Å), and 6724 Å (34 Å), respectively. Bad pixels do not appear in the co-added images because adjacent exposures were shifted by a few seconds of arc with respect to one another. Total exposure times for the [O II], Hα, and [S II] images were 75, 40, and 15 minutes, respectively. Contour plots of the HH 47 region at [S II] and [O II] appear in Figure 3.

The long-slit observations were made with the Manchester echelle spectrometer (Meaburn *et al.* 1984) combined with the 3.9 m Anglo-Australian telescope on the night of 1989 February 15. The slit width was 150 μm wide (1″ on the sky), and the spectral resolution was 9 km s^{-1}. A 90 Å bandwidth interference filter isolated the 87th echelle order, which contained the Hα and [N II] λ6548 and [N II] λ6583 emission lines. The position angle of the slit was 57°. The first slit position went through star B (Figs. 1 and 2), and the second position was offset 4″ north of the first to include the brightest portion of HH 47A. The integration times for positions 1 and 2 were 103 and 67 minutes, respectively. The spectrophotometric standard EG 99 was used to calibrate the absolute fluxes of the observations, which should be accurate to ±10%. Radial velocities were calculated to an accuracy of ±1 km s^{-1} using the comparison Cu-Ar lamp. Position-velocity diagrams of the Hα profiles for the two slit positions appear in Figures 4 and 5.

The [S II] and Hα images in Figure 1 resemble those published previously. The ionization rim around the northern edge of the dark globule is most apparent in the Hα image, with the jet and HH objects brightest in the [S II] image. This behavior is expected, because Hα should be strong along an ionization front, and low-excitation HH objects and jets have prominent [S II] emission. The opposite side of the bipolar flow is visible as a redshifted counterjet in the [S II] image (also Reipurth 1989*b*) and a set of redshifted HH objects (HH 47C) at the southwestern edge of the globule.

The [O II] image differs markedly from the [S II] and Hα images in Figures 1 and 3, and reveals a morphology only hinted at in previous studies of the region. The outer bow-shaped object HH 47D is nearly as bright as HH 47A in [O II], and the bow extends all the way back to the reflection nebula HH 46 near the infrared source. The [O II] emission appears to outline the edges of an expanding shell of material.

The heliocentric radial velocity of the cloud is about +22 km s^{-1} (Kuiper *et al.* 1987; de Vries *et al.* 1984), close to the velocity of the ambient Hα emission throughout the area (Graham and Elias 1983; Figs. 4 and 5). Both position-velocity diagrams have prominent Hα emission along the entire length of the slit near the systemic velocity. The ambient Hα emission comes from the ionization rim around the globule and from the H II region ionized by the nearby O stars ζ Pup and γ^2 Vel. The emission becomes weaker and shifts to more negative radial velocities (∼ +15 km s^{-1} heliocentric) near the globule. The observed line width of the ambient emission is 20 km s^{-1}, consistent with thermal broadening. The vertical feature just left of center in Figure 4*a* is the spectrum of star B, also marked in Figures 1 and 2.

The remaining emission in the position-velocity diagrams (Figs. 4 and 5) is associated with the HH 46/47 outflow. The vertical feature at the right-hand edge of both displays is scattered Hα emission from the infrared source that drives the HH objects. A reflection nebula is visible at this position in broad-band images of the region (Graham and Elias 1983). Emission at $V_{HEL} = -150$ km s^{-1} between HH 47A and the infrared source is visible in slit position 1 but not in position 2 (Figs. 4 and 5). This emission comes from the jet, and extends all the way from the reflection nebula to HH 47A in a long-slit spectrum of [S II] by Meaburn and Dyson (1987). The presence or absence of emission from the jet depends critically on the slit position. In contrast, the appearance of the extended HH object HH 47D is quite similar in the two sets of observations, showing a striking "hook-shaped" position-velocity profile. The emission from HH 47A is broad (∼110 km s^{-1}) and considerably blueshifted from the systemic velocity of the cloud.

We see no kinematic evidence for a curved secondary jet (indicated by a dashed line in Fig. 2) suggested by Glencross *et al.* (1989). The existence of a secondary jet is suspect. Jets interacting with the surrounding medium produce bright [S II] emission like that seen along the main jet in this system. In contrast, the curved feature referred to by Glencross *et al.* (1989) is brightest in the Hα image. The object appears to be a continuation of the arc-shaped reflection nebula surrounding the infrared source. The reflection nebula has a strong component of Hα emission (Figs. 4 and 5).

III. SHOCK MODELS FOR HH 47D AND HH 47A

Although theoretical position-velocity profiles expected from bow shocks exist in the literature (e.g., Raga and Böhm 1986), none are applicable to the current data set. The bow shock models described by HRH can be used to predict position-velocity diagrams. The models partition the bow shock into a series of annuli, each with a size, velocity, and set of emission-line fluxes specified by the shock velocity, viewing angle, and shape of the bow shock. The addition of an entrance slit to the problem alters the observed velocity profile by excluding a fraction of the emission from each annulus (see Fig. 2 of HRH).

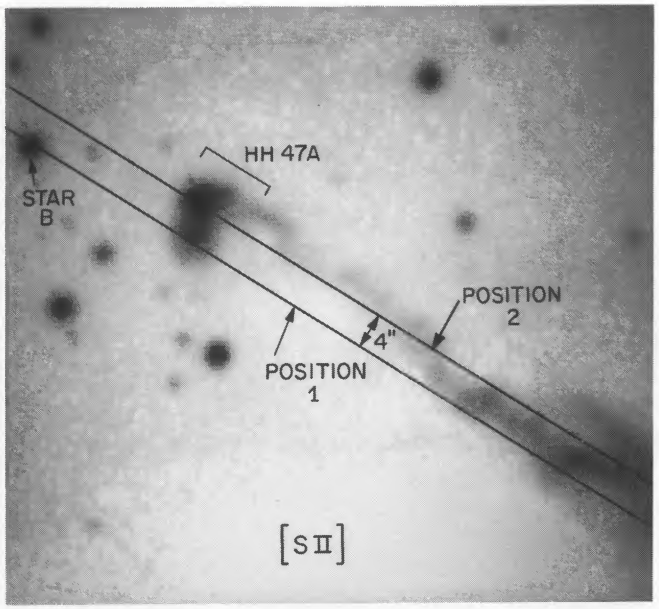

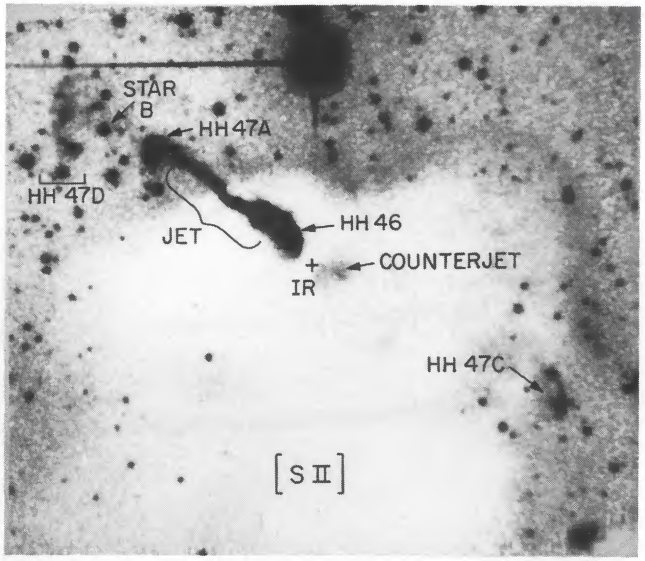

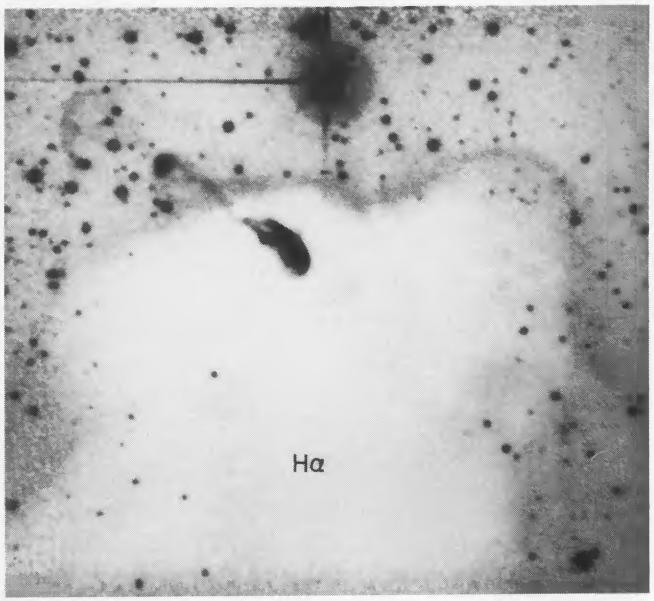

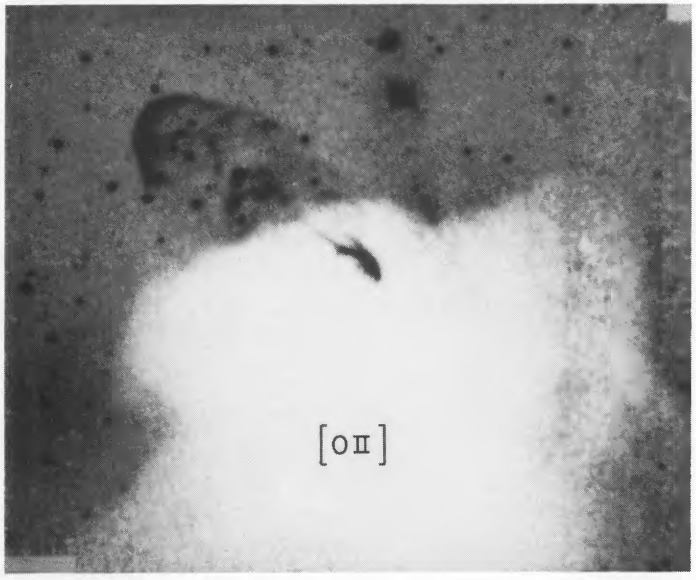

FIG. 1.—[S II], Hα, and [O II] images of the HH 46/47 system. The slit positions used for the echelle observations are indicated in the enlargement of the [S II] image, which has been scaled to show the shape of HH 47A. The [S II] image has a prominent jet and a counterjet, the Hα image displays a bright ionization rim around the globule, and the [O II] image reveals an extended outer bow shock that is visible only weakly in other images of this object. The position of the infrared source is indicated by a plus sign.

HARTIGAN, RAYMOND, AND MEABURN (*see* **362**, 625)

PLATE 29

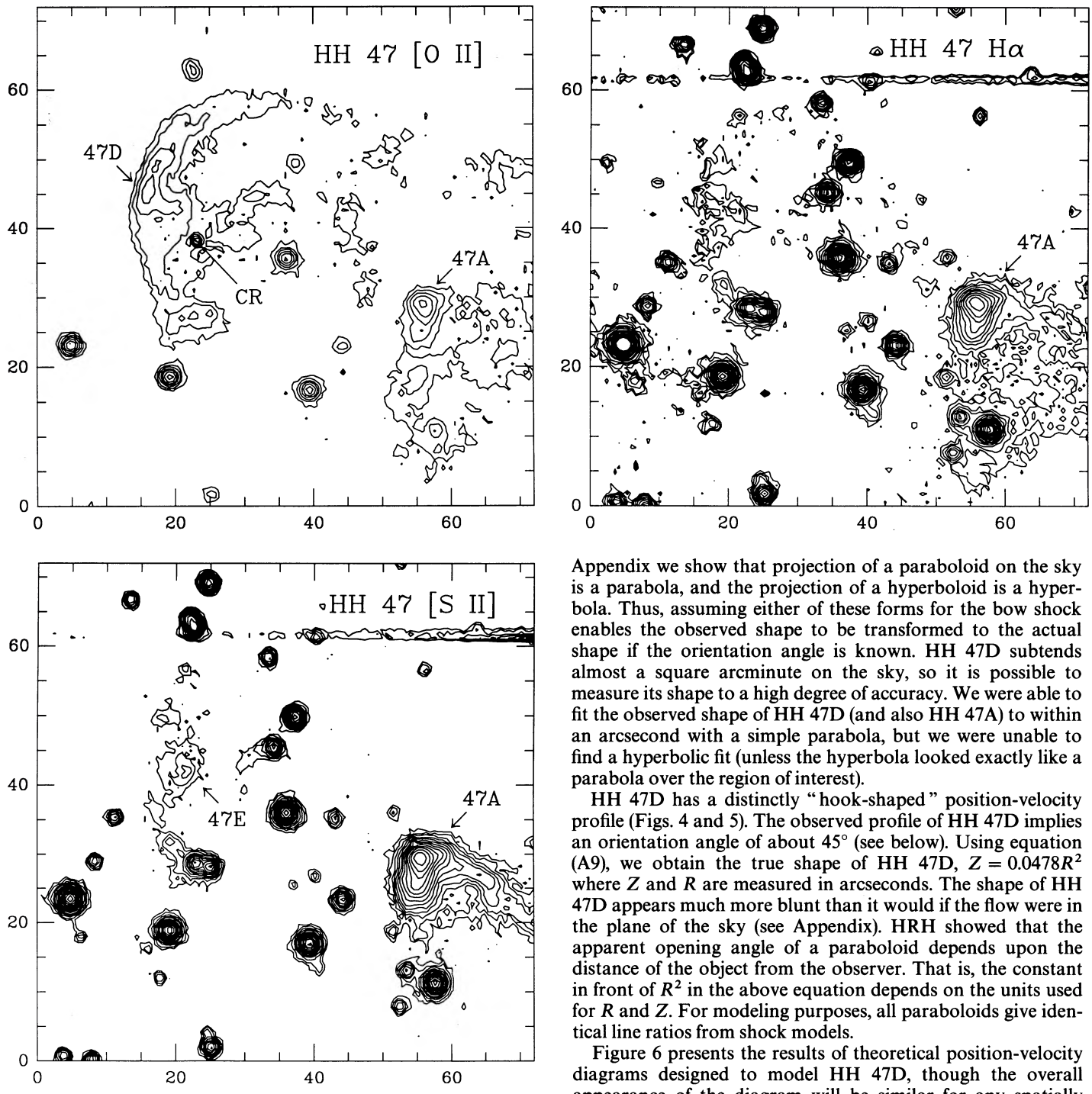

FIG. 3.—Contour plots of the images in Fig. 1 near HH 47. HH 47A is clearly bow-shaped in all three images, but the outer blow shock HH 47D is visible easily only in [O II]. A low-excitation knot ("E") could represent the Mach disk of the outer bow shock or a third major ejection from the infrared source. "CR" denotes a prominent cosmic-ray hit in the [O II] image. The contours are logarithmic, with a factor of 1.41 between adjacent contours. The x-axis and the y-axis have units of arcseconds and the images are aligned with each other to within 0.″3. North is up and east is to the left.

The shape of the bow shock is one of the input parameters in the model. Raga (1986) proposed a shape that was essentially a sum of a quadratic and a quartic, and HRH parameterized this shape to include arbitrary quadratic and quartic shapes. In the Appendix we show that projection of a paraboloid on the sky is a parabola, and the projection of a hyperboloid is a hyperbola. Thus, assuming either of these forms for the bow shock enables the observed shape to be transformed to the actual shape if the orientation angle is known. HH 47D subtends almost a square arcminute on the sky, so it is possible to measure its shape to a high degree of accuracy. We were able to fit the observed shape of HH 47D (and also HH 47A) to within an arcsecond with a simple parabola, but we were unable to find a hyperbolic fit (unless the hyperbola looked exactly like a parabola over the region of interest).

HH 47D has a distinctly "hook-shaped" position-velocity profile (Figs. 4 and 5). The observed profile of HH 47D implies an orientation angle of about 45° (see below). Using equation (A9), we obtain the true shape of HH 47D, $Z = 0.0478R^2$ where Z and R are measured in arcseconds. The shape of HH 47D appears much more blunt than it would if the flow were in the plane of the sky (see Appendix). HRH showed that the apparent opening angle of a paraboloid depends upon the distance of the object from the observer. That is, the constant in front of R^2 in the above equation depends on the units used for R and Z. For modeling purposes, all paraboloids give identical line ratios from shock models.

Figure 6 presents the results of theoretical position-velocity diagrams designed to model HH 47D, though the overall appearance of the diagram will be similar for any spatially resolved bow shock. The line chosen is Hα, using a 1″ wide slit and 2″ seeing for the model bow shock described above. The results are plotted for various viewing angles ϕ, where $\phi = 90°$ is for a bow shock moving perpendicular to the observer and $\phi = 0°$ represents a bow shock moving directly toward the observer. The profiles are symmetrical in velocity when $\phi = 90°$, because at this orientation the front and back sides of the bow shock have opposite radial velocities. The profile is symmetrical with respect to position when $\phi = 0°$ for an axially symmetrical bow shape like the one considered here. At intermediate angles the profile changes shape to produce a distinctive "hook" shape when $\phi \sim 45°$, in excellent agree-

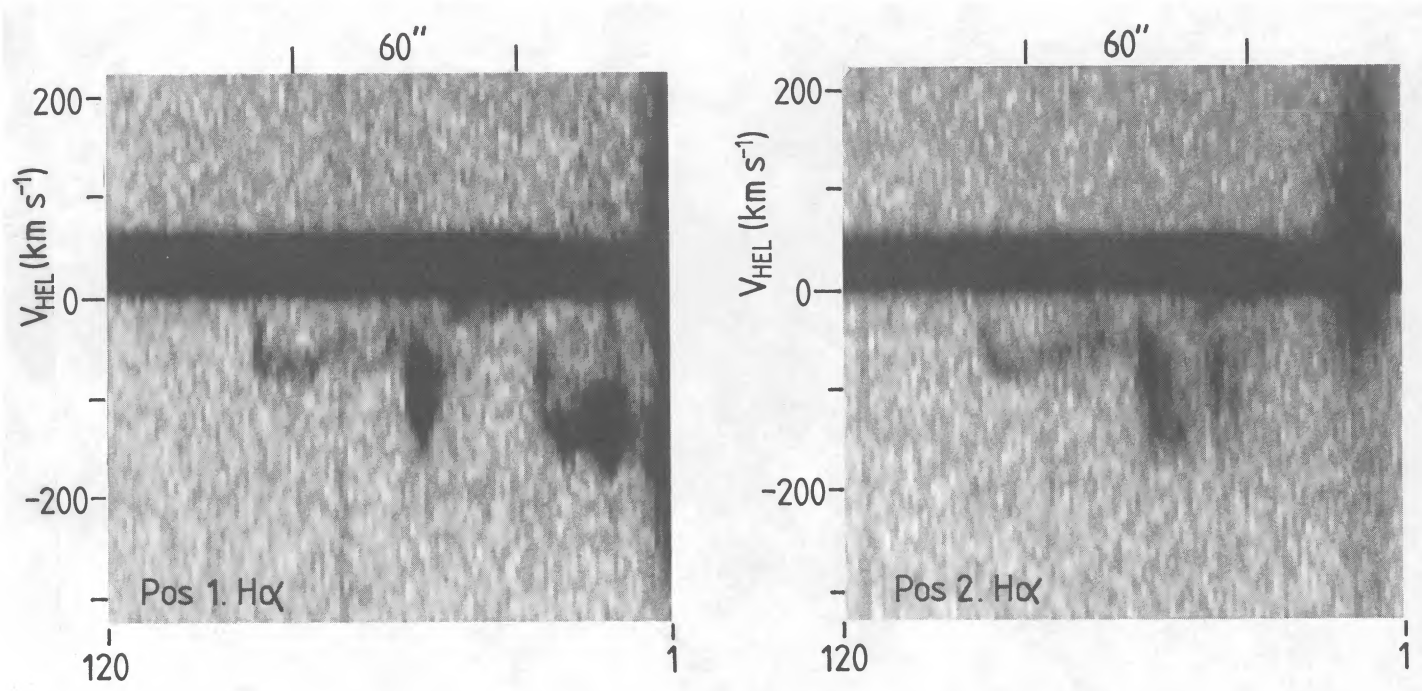

FIG. 4.—(*a*, *b*) Gray-scale representations of the position-velocity diagrams observed for Hα along the two slit positions indicated in Figs. 1 and 2. Position along the slit is depicted along the *x*-axis, with heliocentric radial velocity plotted on the *y*-axis. The vertical feature just left of center in (*a*) is the spectrum of star B, also marked in Figs. 1 and 2. The systemic velocity of the cloud is $+22$ km s^{-1}. Bright emission from the ionization rim around the globule and the surrounding Gum Nebula is prominent along the entire slit for both positions near the systemic velocity. The extended vertical feature at the right-hand edge of both displays is scattered Hα emission from the infrared source that drives the HH objects. The position-velocity diagram of HH 47D shows a distinct "hook-shaped" profile characteristic of a spatially resolved bow shock. The emission from HH 47A is over 100 km s^{-1} wide and is blueshifted with respect to the systemic velocity.

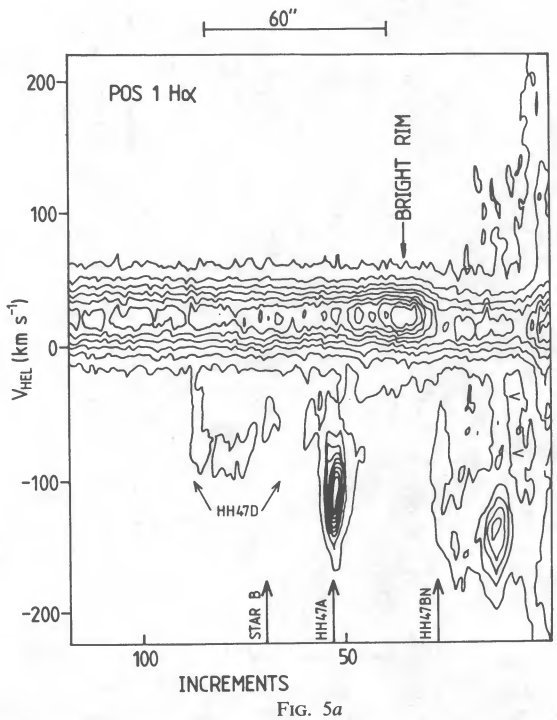

FIG. 5*a*

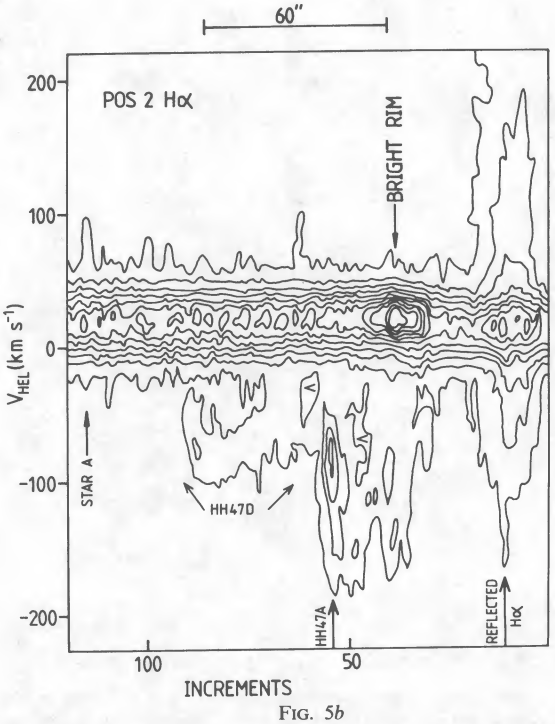

FIG. 5*b*

FIG. 5.—(*a*, *b*) Same as Fig. 4, except that a linear contour representation is used for the data. The lowest contours for positions 1 and 2 are 1.09×10^{-5} and 9.4×10^{-6} ergs s^{-1} cm^{-2} sr^{-1} Å^{-1}, respectively, and the corresponding contour intervals are 0.85×10^{-5} and 0.94×10^{-5} ergs s^{-1} cm^{-2} sr^{-1} Å^{-1}. No corrections for interstellar extinction have been applied to these data.

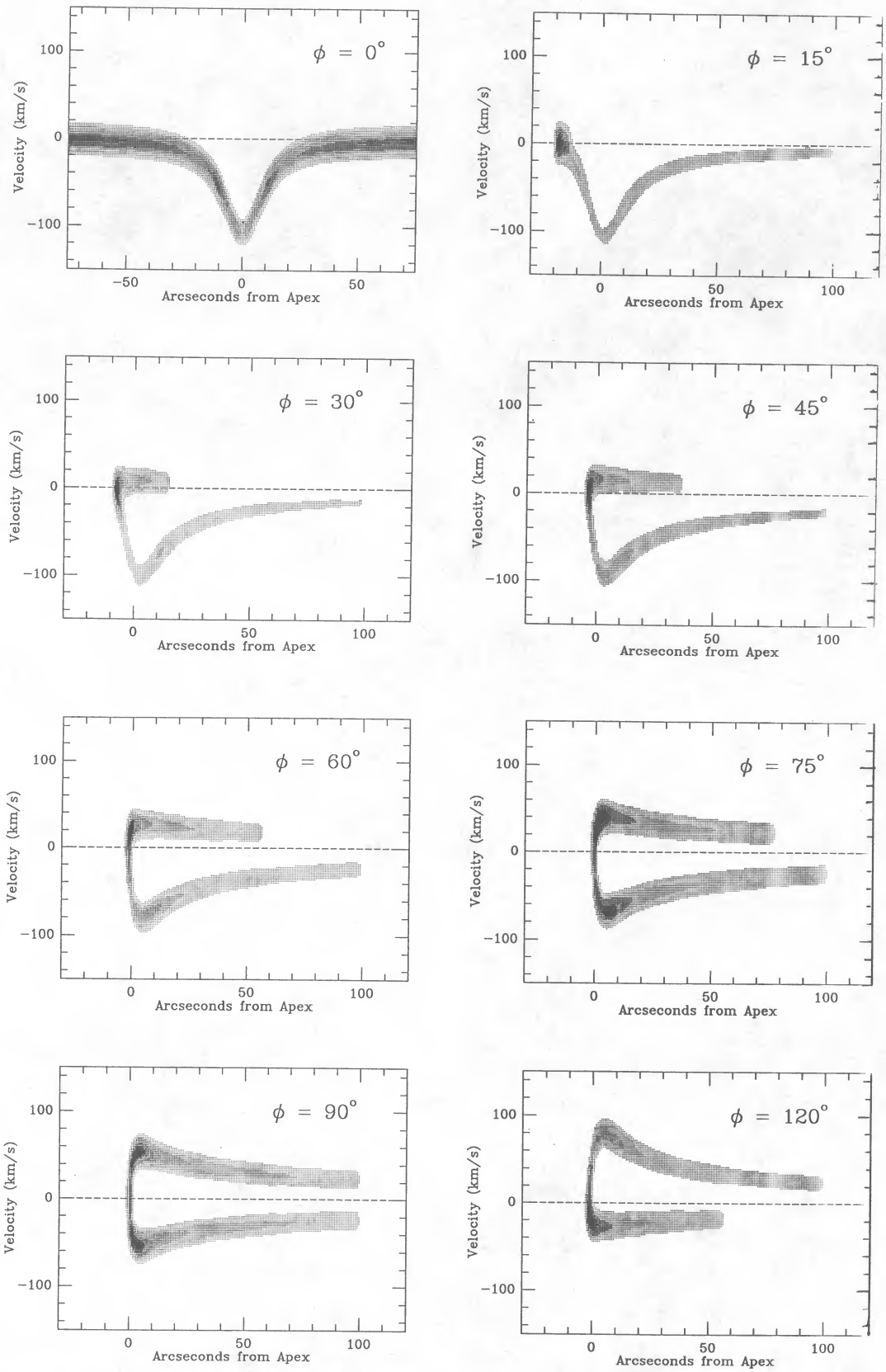

FIG. 6.—Model position-velocity diagram for HH 47D. The model is a 110 km s^{-1} bow shock moving into a fully preionized medium. The bow shape was measured from the images in Fig. 1 and used in the calculations as described in the Appendix. The models show the effect of a changing viewing angle ($\phi = 90°$ is a bow shock moving in the plane of the sky; $\phi = 0°$ is a bow shock moving directly toward the observer). Linear gray scales are plotted in units of 0.1 of the peak intensity. The profiles change markedly as the orientation angle varies, becoming "hook-shaped" for $30° \lesssim \phi \lesssim 60°$, in good agreement with the observed profiles in Figs. 4 and 5. Although these profiles were designed to reproduce the slit size, seeing, and bow shape of HH 47D, the overall shape of the profile will be similar for any well-resolved radiating bow shock.

TABLE 1

OBSERVED AND MODEL OPTICAL LINE RATIOS FOR HH 47A AND HH 47D

Line	Model 47A	Observed 47A[a]	Model 47D	Observed 47D[a]
[O II] λλ3726, 3729	131	107	452	1881
[S II] λ4072	21	94	14	...
Hβ λ4861	100	100	100	100
[O III] λ5007	18	...	21	184
[N I] λ5200	81	119	22	99
[O I] λ6300	177	262	20	264
Hα λ6563	372	372	305	512
[N II] λ6583	59	53	75	319
[S II] λλ6716, 6731	212	727	109	1028

[a] Observed line ratios from Dopita, Schwartz, and Evans 1982 dereddened according to a standard extinction law to make the observed and model Hα/Hβ ratios for HH 47A coincide. The logarithmic reddening constant is 0.37, corresponding to $A_V = 0.81$. The model line ratios are for a 110 km s^{-1} bow shock with a full preionized medium for HH 47D and a 110 km s^{-1} bow shock with an equilibrium preionized medium for HH 47A (cf. HRH). The model line ratios are integrated over the entire bow shock. Emission from the Gum Nebula contaminates the observed line ratios (especially for HH 47D), making comparisons with the models difficult.

ment with the observed position-velocity profiles in Figures 4 and 5. A 110 km s^{-1} bow shock moving into a stationary medium with $\phi \sim 45°$ provides a good match to the observed spatial and velocity characteristics of HH 47D. The optical and ultraviolet line ratios obtained integrating over the entire bow shock, using a 110 km s^{-1} shock and a fully preionized preshock medium for HH 47D, are given in Tables 1 and 2. The most striking numbers in this table are the large [O II] line fluxes and the relative weakness of the other lines. This is in agreement with the images in Figure 1, which show strong [O II], and detectable, but less prominent, emission from [S II] and Hα in HH 47D.

The morphology of HH 47A also resembles a bow shock in Figures 1 and 3. The brightness of HH 47A in Figures 1 and 3 decreases most rapidly to the northeast (in the direction of the flow), characteristic of a bullet or jet geometry and not a "shocked cloudlet" geometry (Raga 1986). The observed line width of HH 47A in Figures 4 and 5 (the position that passes through the apex of the bow) is similar to that of HH 47D, so the bow shock velocity for HH 47A must also be about 110 km s^{-1}. A bow shock model with a stationary ambient medium will not explain the observations of HH 47A, however, because any such model must include zero radial velocity within the line profile (HRH). The model of HH 47A in Figure 7 is for a bow shock with the axis of symmetry tilted 45° from the line of sight and moving into a medium with an outward velocity of 90 km s^{-1}. The model [S II] profile shows a "tail" of emission extending behind the apex of the bow shock at a radial velocity of −80 to −100 km s^{-1}. This tail is not as prominent in higher excitation lines like Hα because it arises from the wings of the bow shock where the shock is oblique.

The geometry of a bow shock controls the overall shape of a position-velocity diagram (such as the "tail" of emission described above) for a given viewing angle. The intensities in a position-velocity diagram are more uncertain because these depend upon the relative sizes of the slit and bow shock, the

TABLE 2

MODEL ULTRAVIOLET LINE RATIOS FOR HH 47A AND HH 47D (Hβ = 100)

Line	Model 47A	Model 47D
C II λ1336	56	93
C IV λ1549	21	21
He II λ1640	1	52
O III] λ1663	9	10
Si III] λ1891	31	72
C III] λ1908	46	48
C II] λ2326	128	112
Mg II λ2799	263	167

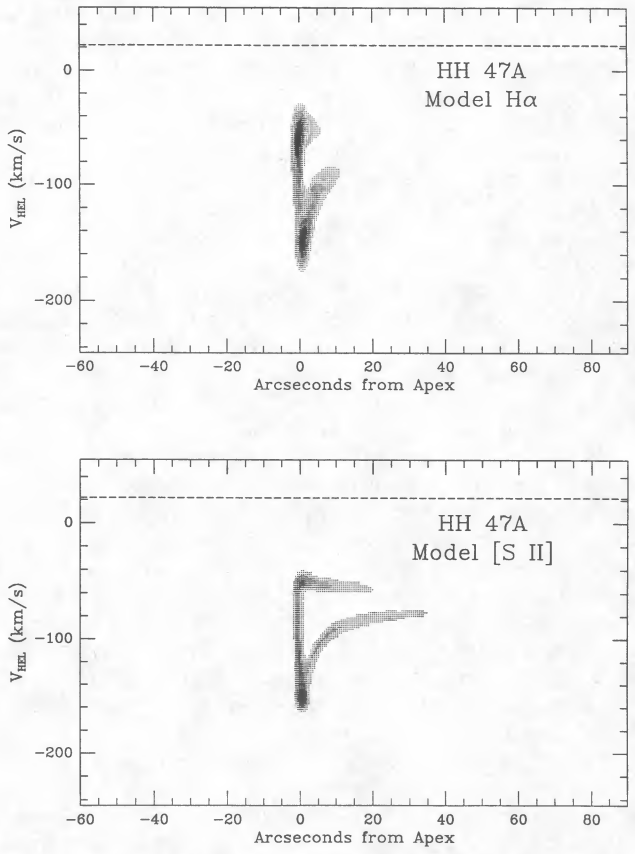

FIG. 7.—Same as Fig. 6, but using an equilibrium preionized medium and the bow shape measured for HH 47A. The viewing angle is 45°, with the preshock medium moving outward at 90 km s^{-1} (see text). The [S II] line profile shows an extended "tail" at $V_{HEL} \sim -80$ km s^{-1}. The dotted line shows the systemic velocity of the molecular cloud.

amount of velocity broadening, the preshock ionization conditions, the seeing, and the emissivities used in the planar shock models. *Any* bow shock model of a low-excitation emission line (such as [S II]) observed at $\phi \sim 45°$ with a slit narrower than the bow shock will have a tail of emission near the radial velocity of the preshock medium (in this case $V_{\rm HEL} \sim -80$ km s^{-1}). Meaburn and Dyson (1987) see a tail in their [S II] (but not Hα) spectra of HH 47A, and referred to it as the low-velocity component of a "velocity ellipse." The high-velocity portion of the ellipse ($V_{\rm HEL} \sim -170$ km s^{-1}) is bright in [S II] and extends most of the way back to the exciting source as a low-excitation jet. The high-velocity material probably arises from oblique shocks across the outflowing jet, because oblique shocks provide the large radial velocities, low-excitation spectra, and narrow line widths observed by Meaburn and Dyson. Emission from the jet is displaced an arcsecond or two to the north of the axis of symmetry of HH 47A. No simple axially symmetric model can explain this offset.

The observed line ratios for HH 47A and HH 47D must have the ambient emission from the surrounding Gum Nebula subtracted, and then must be dereddened to compare with the models. We dereddened the line fluxes of Dopita, Schwartz, and Evans (1982) by requiring that the dereddened Balmer decrement match the model decrement for HH 47A, where background contamination will be much fainter than emission from the object. We chose a 110 km s^{-1} bow shock with a preshock medium in steady state with the emerging ionizing photons to model HH 47A (an "equilibrium" preionized model; cf. HRH). The predicted line ratios agree quite well with the observations of HH 47A, although the model [S II]/Hβ ratio is too low. It is possible that a weak Mach disk shock is present within HH 47A, and this shock could increase the line fluxes of low ionization species like [S II]. The equilibrium preionization models tend to overestimate the amount of ionization in front of a curved shock (Raymond, Hartigan, and Hartmann 1988). A more quantitative treatment of the preshock ionization would also tend to increase the [S II]/Hβ line ratio in HH 47A.

Contaminating emission from the Gum Nebula is particularly worrisome in HH 47D, which is very faint. For this reason we did not attempt to deredden the HH 47D line fluxes from the observations, but instead employed the reddening correction derived for HH 47A. The resulting line ratios in Table 1 are quite peculiar, and have a large Balmer decrement and very large [S II] λ6720/Hβ and [O II] λ3727/Hβ line ratios. In general, the agreement with the model is rather poor, but spectrophotometric observations of the region with careful background subtraction are needed to verify the discrepancies.

We predict that any [O III] emission from HH 47A will be weak, in agreement with the observations of Dopita (1978) and Dopita, Evans, and Schwartz (1982). HH 47A is visible very faintly in an [O III] image we obtained of the region, but there is a neighboring Fe II emission line at 5018 Å that falls within the bandpass of the filter, so we cannot detect the presence of [O III] definitively from our images alone. The presence or absence of [O III] emission in a shock model depends critically upon the shock velocity. For example, a 100 km s^{-1} bow shock model produces an [O III] λ5007/Hβ line ratio of 0.07 instead of the 0.18 for the 110 km s^{-1} model in Table 1, and fits the line profiles as well as the 110 km s^{-1} model.

IV. DISCUSSION

The morphology of the HH 47 outflow suggests a geometry where HH 47D represents the bow shock of the jet and HH 47A is the Mach disk (also called the "working surface"; Meaburn and Dyson 1987). The prominent jet in HH 46/47 appears to end in a bright knot, HH 47A, with HH 47D displaced some 43″ further along the outflow axis (Figs. 1 and 3). Hartigan (1989) examined the existing velocity and density measurements of the region and concluded that a simple continuous jet with a bow shock (HH 47D) and Mach disk (HH 47A) configuration could only account for the observations if HH 47D was partially radiative.

The jet model can be reexamined in light of the observations presented in this paper. From the images in Figures 1 and 3 it is clear that [O II] radiates over the entire bow shock. The shock models in Table 1 indicate that the medium exterior to the globule is ionized (see also Dopita, Schwartz, and Evans 1982), not because the apex of the bow shock is nonradiative. The shock velocity of the outer bow shock HH 47D is 110 ± 15 km s^{-1} from the observed position-velocity diagrams in Figures 4 and 5 and the model profiles in Figure 6. The sharp decline in radial velocity at the apex of HH 47D restricts $\phi \gtrsim 35°$, and the lack of redshifted emission from HH 47D implies $\phi \lesssim 55°$. The observed radial velocity of the jet with respect to the exciting source is 165 km s^{-1} (Meaburn and Dyson 1987), so the actual jet velocity lies between 200 and 280 km s^{-1} for the allowed range of viewing angles. Thus, the shock velocity of the Mach disk should lie between 90 and 170 km s^{-1} for a continuous jet model. The continuous jet model can just explain the lack of strong [O III] emission from HH 47A as long as the shock velocity of the Mach disk is close to 90 km s^{-1}.

However, the surface brightnesses, spatial separation, and densities of HH 47A and HH 47D are *not* consistent with a continuous outflowing jet where HH 47A is the Mach disk and HH 47D the bow shock. The surface brightness of HH 47A in Figure 1 is about 50 times that of HH 47D in Hα. The flux from a radiative shock at Hα increases linearly with the preshock density and roughly quadratically with the shock velocity (HRH; Cantó and Rodríguez 1986). The ram pressure (ρV^2) of material flowing into the outer bow shock balances the ram pressure of jet gas flowing through the Mach disk to within a factor of 2 or so for a continuous jet (cf. eq. [2] of Hartigan 1989). Thus, the continuous jet model predicts that HH 47A and HH 47D should have comparable surface brightnesses in Hα.

In addition, a continuous jet model cannot explain the spatial separation of HH 47A and HH 47D. The spatial displacement of the Mach disk and bow shock of a jet is on the order of the radius of the jet or the cooling distance behind the shocks, whichever is larger. The cooling distance behind a 110 km s^{-1} shock with a preshock density of 100 cm^{-3} is about 20 AU (HRH). The jet radius is about 4″ for HH 47, corresponding to 1800 AU for a distance to the system of 450 pc (Graham and Heyer 1989). The projected distance between HH 47A and HH 47D should be about 3″ ($R_{\rm jet} \sin \phi$), much smaller than the observed 43″ offset.

The density of the jet is 120 cm^{-3} from the red [S II] line ratio (Meaburn and Dyson 1987). Using this value for n_j in equation (2) of Hartigan (1989) together with 110 km s^{-1} for the bow shock velocity and 200 km s^{-1} $\lesssim V_j \lesssim$ 280 km s^{-1} for the jet velocity, we find the density of the ambient medium exterior to the globule to lie between 55 and 200 cm^{-3} for a continuous jet model. A density this large for the exterior of the globule seems unreasonable in light of the low extinction there (a number of background stars shine through HH 47D in Figs. 1 and 3).

Another possibility is that a stationary Mach disk forms as a result of the density contrast between the interior and the exterior of the globule. In this model the jet is pressure-confined within the globule and becomes an underexpanded jet as it encounters the tenuous external medium exterior to the globule. The subsequent reconfinement of the jet could produce a stationary Mach disk which might be identified with HH 47A. However, these configurations apparently produce only small Mach disks and do not significantly decelerate the flow for large Mach numbers (Chang and Chow 1974). Cantó, Raga, and Binette (1989) have found that crossing shocks in underexpanded jets have effective shock velocities of ~ 20 km s^{-1} independent of the parameters of the jet and the ambient medium. Crossing shocks therefore should not produce bright Hα emission like that seen in HH 47A, and are unlikely to generate the 100 km s^{-1} line width in HH 47A. The large proper motion of HH 47A (160 km s^{-1}; Schwartz, Jones, and Sirk 1984) is difficult to reconcile with this model.

The images and spectra *can* be explained with a jet model that is episodic. Such a model was originally suggested by Dopita (1978) for this region, and has been used more recently by Reipurth (1989*b*) in connection with observations of HH 111. If the jet is episodic, then one would expect a bow shock to form each time the star ejects a new stream of material. With this picture, both HH 47D and HH 47A are bow shocks, in agreement with the overall morphologies in Figures 1 and 3.

Each bow shock will have its own Mach disk as long as material from the ejection collides with the back of the bow shock. There is evidence for the existence of a Mach disk in HH 47D in Figures 1 and 3. The [S II] and Hα images of HH 47D have weak emission at the position of the bow shock in the [O II] image, but there is an additional emission knot located about 7″ closer to the infrared source that has a much lower excitation spectrum than the outer bow shock. This knot (labeled "E" in Fig. 3) is brighter than the outer bow shock by a factor of 4 or so at [S II], but the surface brightnesses of knot E and the outer bow shock are comparable at Hα. A lower excitation spectrum for knot E compared with the outer bow shock is what would be expected of a Mach disk if the density of the jet is larger than the ambient medium, as is the case in HH 47 (Hartigan 1989). Knot E could also represent a third ejection from the infrared source.

Most important, the *kinematics* of the observed gas are consistent with a multiple ejection model for HH 47. A second ejection (HH 47A) will run into the wake of the initial flow (HH 47D) and produce a bow shock that moves into an outwardly flowing medium. The spectra of HH 47A (§ III) do not include zero radial velocity within the line profiles, characteristic of a bow shock moving into an outflowing medium. The value of 90 km s^{-1} for the velocity of the medium in front of HH 47A used in the model (Fig. 7; § III) was chosen to match the observed line width and velocity of HH 47A but is also in excellent agreement with the velocity expected for gas behind HH 47D. Material in the wake of HH 47D should flow outward at a large fraction of the full shock velocity (110 km s^{-1}) for a radiative shock. In a multiple ejection model HH 47A should move at a velocity ~ 200 km s^{-1} with respect to the infrared source if $\phi \sim 45°$. The observed proper motion of HH 47A (160 km $s^{-1} \pm 30\%$) and the predicted value (140 km s^{-1}) agree to within the observational errors in a multiple ejection model.

The presence of multiple ejections from embedded young stars is not surprising in light of recent ideas about accretion and outflow from young stars. The sudden brightening of pre–main-sequence objects known as FU Orionis variables has been attributed to the onset of an eruptive episode of disk accretion (e.g., Kenyon and Hartmann 1988). Disk accretion onto normal T Tauri stars also varies considerably from night to night (e.g., Hartigan *et al.* 1990). The relationship of accretion to outflow is unclear, but there is some observational evidence that stars undergoing more rapid disk accretion also drive more energetic winds (Cabrit *et al.* 1990; Hartigan *et al.* 1990). Hence, multiple ejections from a newly formed star could arise from multiple accretion events within a dense circumstellar disk around the young star. Assuming ballistic flow and a viewing angle $\phi = 45°$, the time elapsed between the HH 47D and HH 47A ejections is about 2000 years.

A combination of a disk wind and a stellar wind is another viable model for the HH 47 outflow. In this model the region bounded by the outer bow shock HH 47D is filled with a poorly collimated disk wind, and a highly collimated jet from a stellar wind produces the bow shock HH 47A. Although this model differs conceptually from a multiple ejection model, the two scenarios are similar kinematically in that both have a high-velocity collimated flow moving through a less collimated, slower flow. A similar model has been used by Stocke *et al.* (1988) to explain the Herbig-Haro objects in the L1551 outflow.

Raga *et al.* (1987) have suggested that thermal instabilities play an important role in forming the condensations seen within HH 1. However, thermal instabilities cannot produce the clumpiness in HH 47D because the shock velocity of 110 km s^{-1} is lower than that required for the onset of thermal instabilities (Innes, Giddings, and Falle 1987). The [O II] image of HH 47D in Figure 1 shows a clumpy structure at a factor of 2 level in intensity. Inhomogeneities in the preshock medium will produce nonuniform emission in a bow shock, as will Rayleigh-Taylor instabilities acting between hot jet gas and cooler gas in front of the bow shock (Blondin, Königl, and Fryxell 1989).

V. CONCLUSIONS

HH 46/47 is an isolated outflow that can be studied with high spatial and spectral resolution, making this system ideal for a kinematical study. We have presented Hα, [S II], and [O II] images of this region together with high-resolution echelle spectra along the jet. The [O II] image reveals an extended shell structure (HH 47D) only hinted at in other emission lines. The shell appears to outline the boundary of the outflow from the infrared source. The Hα and [S II] images show the same overall features seen in previously published images (e.g., Graham and Elias 1983; Reipurth 1989*b*), including an ionization rim that is bright in Hα and a low-excitation jet and counterjet emanating from the embedded infrared source.

The two long-slit echelle spectra taken along the axis of the outflow show a "hook-shaped" feature in the position-velocity diagram of HH 47D. Theoretical position-velocity diagrams for a spatially resolved bow shock reproduce the observations of HH 47D remarkably well for a viewing angle $\sim 45°$ and a shock velocity of 110 km s^{-1}. The low-excitation object HH 47A is distinctly bow-shaped, and the line ratios, line profiles, and proper motion of this object agree well with a bow shock that moves into an outward-flowing medium. The velocity of the outflowing medium needed to match the observations is about 90 km s^{-1}, consistent with the expected velocity of material in the wake of HH 47D.

A simple continuous jet model cannot explain the observa-

tions in this system. In fact, the images and the observed position-velocity diagram show clear evidence for *two* spatially resolved bow shocks, with HH 47A plowing into the wake of the larger bow shock HH 47D. Two bow shocks within a single outflowing lobe can occur if the outflow is episodic, or if a highly collimated fast (stellar) wind collides with a slower, less collimated (disk) wind.

P. H. and J. R. would like to thank the staff of CTIO for their cheerful support throughout the observing run. J. M. wishes to thank the staff at the Anglo-Australian telescope for their excellent assistance in 1989 February when the velocity measurements were done. P. H. acknowledges useful discussions with J. Blondin about the nature of jets.

APPENDIX

In what follows we show that the projection of a paraboloid on the sky is a parabola, and the projection of a hyperboloid is a hyperbola. This result can be used to obtain the actual shape of a bow shock, given the viewing angle and the observed shape on the sky.

The equation of a paraboloid surface is

$$F(x, y, z) = \alpha x^2 + \alpha y^2 - z = 0 , \tag{A1}$$

where α is a positive constant and the axis of symmetry of the paraboloid is the z-axis. The axial symmetry of the problem allows us to place the observer in the $(y\,z)$-plane. If an observer at infinity views the paraboloid at an angle ϕ from the negative z-axis, then the unit normal vector along the line of sight is

$$\hat{s} = (\sin\phi)\hat{y} + (\cos\phi)\hat{z} . \tag{A2}$$

The gradient of $F(x, y, z)$ specifies the normal vector to the surface at each point,

$$\nabla F(x, y, z) = 2\alpha x\hat{x} + 2\alpha y\hat{y} - \hat{z} . \tag{A3}$$

The projection of the paraboloid on the sky is given by those points on the paraboloid that are tangent to the line of sight. Hence,

$$\nabla F(x, y, z) \cdot \hat{s} = 0 \Rightarrow 2\alpha y = \cot\phi \qquad (\phi \neq 0) \tag{A4}$$

for the tangent points.

Consider a plane P that passes through the origin and has a unit normal vector $\hat{s}$ given by equation (A2). The projection of the tangent points in equation (A4) onto P gives the observed shape of the paraboloid on the sky. Define a primed coordinate system by rotating the unprimed system through an angle ϕ around the $\hat{x}$-axis to make the (x', z')-plane coincide with P. Then

$$\hat{x}' = \hat{x} , \qquad \hat{y}' = \hat{s} = (\sin\phi)\hat{y} + (\cos\phi)\hat{z} , \qquad \hat{z}' = -(\cos\phi)\hat{y} + (\sin\phi)\hat{z} . \tag{A5}$$

The coordinates of a point (x', y', z') transform to (x, y, z) according to the relations

$$x' = x , \qquad y' = y\sin\phi + z\cos\phi , \qquad z' = -y\cos\phi + z\sin\phi \tag{A6}$$

and

$$x = x' , \qquad y = y'\sin\phi - z'\cos\phi , \qquad z = y'\cos\phi + z'\sin\phi . \tag{A7}$$

Combining the equations for z', z, y', and y in equations (A6) and (A7) with the expression for y of the tangent points to the surface in equation (A4) gives

$$z = z'\csc\phi + \frac{\cot^2\phi}{2\alpha} . \tag{A8}$$

Substituting the expression for y in equation (A4) into the equation for the paraboloid (A1) and using equation (A8), we obtain

$$z' + \frac{\cot\phi\cos\phi}{4\alpha} = (\alpha\sin\phi)x'^2 . \tag{A9}$$

Equation (A9) is the projection of the paraboloid onto the plane of the sky. The shape is a parabola. The projection becomes wider (and more offset from the origin) as the paraboloid is viewed more obliquely.

In a similar manner one can show that the projection of the hyperboloid

$$F(x, y, z) = \frac{z^2}{a^2} - \frac{y^2}{b^2} - \frac{x^2}{b^2} - 1 = 0 \tag{A10}$$

is the hyperbola

$$\frac{z'^2}{a'^2} - \frac{x'^2}{b'^2} = 1 , \tag{A11}$$

with $a' = a\sin\phi\,[1 - (b^2/a^2)\cot^2\phi]^{1/2}$ and $b' = b$. The hyperbolic projection also becomes wider as the viewing angle ϕ deviates

from 90°. A hyperboloid has the interesting property that the Mach number of the flow determines the shape of the shock at large distances from the apex of the bow (the asymptotes define the Mach angle). As in the case of parabolae, there are families of shapes that are essentially the same for modeling purposes. All hyperboloids with the same ratio a/b (the same Mach number) give identical line ratios and line profiles. Hyperboloids with the same ratio a/b can be thought of as being the same shape viewed from different distances. Although the hyperboloid is an attractive shape because of these properties, the observed shape of the HH objects studied in this paper can be reproduced with a paraboloid but not with a hyperboloid (see text).

REFERENCES

Blondin, J. M., Königl, A., and Fryxell, B. A. 1989, *Ap. J. (Letters)*, **337**, L37.
Cabrit, S., Edwards, S., Strom, S. E., and Strom, K. M. 1990, *Ap. J.*, **354**, 687.
Cantó, J., Raga, A. C., and Binette, L. 1989, *Rev. Mexicana Astr. Af.*, **17**, 65.
Cantó, J., and Rodríguez, L. F. 1986, *Rev. Mexicana Astr. Af.*, **13**, 57.
Chang, I. S., and Chow, W. L. 1974, *AIAA J*, **12**, 1079.
de Vries, C. P., Brand, J., Israel, F. P., de Graauw, T., Wouterloot, J. G. A., van de Stadt, H., and Habing, H. J. 1984, *Astr. Ap. Suppl.*, **56**, 333.
Dopita, M. A. 1978, *Astr. Ap.*, **63**, 237.
Dopita, M. A., Binette, L., and Schwartz, R. D. 1982, *Ap. J.*, **261**, 183.
Dopita, M. A., Schwartz, R. D., and Evans, I. 1982, *Ap. J. (Letters)*, **263**, L73.
Emerson, J. P., Harris, S., Jennings, R. E., Beichman, C. A., Baud, B., Beintema, D. A., Marsden, P. L., and Wesselius, P. 1990, *M.N.R.A.S.*, in press.
Glencross, W. M., Cameron, D. H. M., Lightfoot, J. F., and Whitmore, B. 1989, *M.N.R.A.S.*, **238**, 689.
Graham, J. A., and Elias, J. H. 1983, *Ap. J.*, **272**, 615.
Graham, J. A., and Heyer, M. 1989, *Pub. A.S.P.*, **101**, 573.
Hartigan, P. 1989, *Ap. J.*, **339**, 987.
Hartigan, P., Hartmann, L., Kenyon, S. J., Strom, S. E., and Skrutskie, M. 1990, *Ap. J. (Letters)*, **354**, L25.
Hartigan, P., Raymond, J., and Hartmann, L. 1987, *Ap. J.*, **316**, 323 (HRH).
Innes, D. E., Giddings, J. R., and Falle, S. E. A. G. 1987, *M.N.R.A.S.*, **224**, 179.
Kenyon, S. J., and Hartmann, L. 1988, *Ap. J.*, **325**, 231.
Königl, A. 1989, *Ap. J.*, **342**, 208.
Kuiper, T. B. H., Peters, W. L., III, Forster, J. R., Gardner, F. F., and Whiteoak, J. B. 1987, *Pub. A.S.P.*, **99**, 107.
Lada, C. J. 1985, *Ann. Rev. Astr. Ap.*, **23**, 267.
Lind, K. R., Payne, D. G., Meier, D. L., and Blandford, R. D. 1989, *Ap. J.*, **344**, 89.
Meaburn, J., Blundell, B., Carling, R., Gregory, D. F., Keir, D., and Wynne, C. 1984, *M.N.R.A.S.*, **210**, 463.
Meaburn, J., and Dyson, J. E. 1987, *M.N.R.A.S.*, **225**, 863.
Mundt, R., Brugel, E. W., and Bührke, T. 1987, *Ap. J.*, **319**, 275.
Norman, C. A., and Silk, J. 1979, *Ap. J.*, **228**, 197.
Norman, M. L., Smarr, L., and Winkler, K.-H.-A. 1985, in *Numerical Astrophysics*, ed. J. Centrella, J. LeBlanc, and R. Bowers (Boston: Jones & Bartlett), p. 88.
Pudritz, R. E., and Norman, C. A. 1983, *Ap. J.*, **274**, 677.
Raga, A. C. 1986, *A.J.*, **92**, 637.
Raga, A. C., and Böhm, K.-H. 1986, *Ap. J.*, **308**, 829.
Raga, A. C., Mateo, M., Böhm, K.-H., and Solf, J. 1987, *A.J.*, **95**, 1783.
Raymond, J. C., Hartigan, P., and Hartmann, L. 1988, *Ap. J.*, **326**, 323.
Reipurth, B. 1989*a*, *Nature*, **340**, 42.
———. 1989*b*, in *ESO Workshop on Low Mass Star Formation and Pre–Main Sequence Objects*, ed. B. Reipurth (Garching: ESO), p. 247.
Sahu, M., Sahu, K. C., and Pottasch, S. R. 1989, *Astr. Ap.*, **218**, 221.
Scarrott, S. M., and Warren-Smith, R. F. 1988, *M.N.R.A.S.*, **232**, 725.
Schwartz, R. D., Jones, B. F., and Sirk, M. 1984, *A.J.*, **89**, 1735.
Stocke, J., Hartigan, P., Strom, S. E., Strom, K. M., Anderson, E. R., Hartmann, L., and Kenyon, S. J. 1988, *Ap. J. Suppl.*, **68**, 229.

PATRICK HARTIGAN: Department of Astronomy, University of Massachusetts, Amherst, MA 01003

JOHN MEABURN: Department of Astronomy, University of Manchester, Manchester M13 9PL, United Kingdom

JOHN RAYMOND: Harvard-Smithsonian Center for Astrophysics, Mail Stop 16, 60 Garden Street, Cambridge, MA 02138